



Cite this: *Phys. Chem. Chem. Phys.*,  
2024, 26, 5356

# Investigation of Pb–B Bonding in $\text{PbB}_2(\text{BO})_n^-$ ( $n = 0-2$ ): Transformation from Aromatic $\text{PbB}_2^-$ to $\text{Pb}[\text{B}_2(\text{BO})_2]^{-/0}$ Complexes with $\text{B}\equiv\text{B}$ Triple Bonds†

Qiang Chen,<sup>a</sup> Wei-Jia Chen,<sup>b</sup> Xin-Yao Wu,<sup>a</sup> Teng-Teng Chen,<sup>be</sup>  
Rui-Nan Yuan,<sup>a</sup> Hai-Gang Lu,<sup>ac</sup> Dao-Fu Yuan,<sup>bd</sup> Si-Dian Li<sup>\*ac</sup> and  
Lai-Sheng Wang<sup>\*b</sup>

Boron has been found to be able to form multiple bonds with lead. To probe Pb–B bonding, here we report an investigation of three Pb-doped boron clusters,  $\text{PbB}_2^-$ ,  $\text{PbB}_3\text{O}^-$ , and  $\text{PbB}_4\text{O}_2^-$ , which are produced by a laser ablation cluster source and characterized by photoelectron spectroscopy and *ab initio* calculations. The most stable structures of  $\text{PbB}_2^-$ ,  $\text{PbB}_3\text{O}^-$ , and  $\text{PbB}_4\text{O}_2^-$  are found to follow the formula,  $[\text{PbB}_2(\text{BO})_n]^-$  ( $n = 0-2$ ), with zero, one, and two boronyl ligands coordinated to a triangular and aromatic  $\text{PbB}_2$  core, respectively. The  $\text{PbB}_2^-$  cluster contains a  $\text{B}=\text{B}$  double bond and two Pb–B single bonds. The coordination of BO is observed to weaken Pb–B bonding but strengthen the  $\text{B}=\text{B}$  bond in  $[\text{PbB}_2(\text{BO})_n]^-$  ( $n = 1, 2$ ). The anionic  $[\text{PbB}_2(\text{BO})_2]^-$  and its corresponding neutral closed-shell  $[\text{PbB}_2(\text{BO})_2]$  contain a  $\text{B}\equiv\text{B}$  triple bond. A low-lying Y-shaped isomer is also observed for  $\text{PbB}_4\text{O}_2^-$ , consisting of a central  $\text{sp}^2$  hybridized B atom bonded to two boronyl ligands and a PbB unit.

Received 15th June 2023,  
Accepted 11th January 2024

DOI: 10.1039/d3cp02800c

rsc.li/pccp

## 1 Introduction

Three-dimensional (3D) cages, especially the well-known  $\text{B}_{12}$ -icosahedral cage, are key structural features prevalent in boranes and various boron allotropes.<sup>1–3</sup> However, in the past two decades, size-selected boron clusters have been found through systematic experimental and theoretical studies to be planar or quasi-planar (2D) up to very large sizes.<sup>4–10</sup> The first 3D borospherene cage ( $\text{B}_{40}$ ) was discovered in 2014,<sup>11</sup> followed by the axially chiral borospherene  $\text{B}_{39}^-$  in 2015.<sup>12</sup> Subsequently, seashell-like borospherenes were found as minor isomers for the  $\text{B}_{28}^-$  and  $\text{B}_{29}^-$  clusters.<sup>13,14</sup> The largest boron cluster ( $\text{B}_{48}^-$ ),

characterized experimentally to date, was found to have a bilayer-type structure.<sup>15</sup> Significant experimental efforts have also been devoted to investigate metal-doped boron clusters, which have been shown to display a wide variety of novel structural patterns,<sup>10,16–18</sup> such as fan-shaped structures,<sup>19–22</sup> double-chain ribbons,<sup>23,24</sup> metal-centered boron wheels,<sup>16,25–29</sup> half-sandwich structures,<sup>30–35</sup> metallo-borophenes,<sup>8,36,37</sup> metal-centered boron drums,<sup>37–42</sup> metallo-borospherenes,<sup>43</sup> and metal-borazene complexes.<sup>24,44,45</sup> The most important chemical bonding features of boron and metal-doped boron clusters are found to be dominated by both delocalized  $\sigma$  and  $\pi$  bonds as a result of boron's electron deficiency.<sup>6–8,18,46–49</sup>

In addition to forming delocalized bonds, boron is also capable of engaging in localized bonds. For instance, the boronyl group (BO), which is isoelectronic with the cyano group (CN), has been shown to have a strong  $\text{B}\equiv\text{O}$  triple bond<sup>50</sup> and has been synthesized.<sup>51</sup> In fact, even  $\text{B}\equiv\text{B}$  triple bonds have been observed in isolated molecules<sup>52–54</sup> and synthetic compounds.<sup>55</sup> Earlier studies on boron oxide clusters showed that they all contained boronyl ligands<sup>53,56–58</sup> and the analogy between boronyl and H/Au was established, *i.e.* they are all single electron  $\sigma$  donors. Using this analogy, we have designed and observed experimentally many boron-boronyl clusters.<sup>59–64</sup> Recently, several interesting findings have also been made in metal-doped boron oxide clusters that feature unusual metal-boron (M–B) multiple bonds and boronyl ligands. The  $\text{M}\equiv\text{B}$

<sup>a</sup> Institute of Molecular Science, Key Laboratory of Materials for Energy Conversion and Storage of Shanxi Province, Shanxi University, Taiyuan 030006, People's Republic of China. E-mail: lisidian@sxu.edu.cn

<sup>b</sup> Department of Chemistry, Brown University, Providence, Rhode Island 02912, USA. E-mail: laisheng\_wang@brown.edu

<sup>c</sup> Key Laboratory of Chemical Biology and Molecular Engineering of Ministry of Education, Shanxi University, Taiyuan 030006, People's Republic of China

<sup>d</sup> Hefei National Research Center for Physical Sciences at the Microscale, University of Science and Technology of China, Hefei 230026, China. E-mail: ydfu@ustc.edu.cn

<sup>e</sup> Department of Chemistry, The Hong Kong University of Science and Technology (HKUST), Clear Water Bay, Hong Kong SAR, China

† Electronic supplementary information (ESI) available. See DOI: <https://doi.org/10.1039/d3cp02800c>

‡ Q. Chen, W.-J. Chen and X.-Y. Wu contributed equally to this work.

triple bonds were observed in linear  $[M \equiv B-B \equiv O]^-$  ( $M = Bi, Re$ ) and bent  $(^-\text{OB})\text{Ir} \equiv B$ ,<sup>65,66</sup> while the bent  $(^-\text{OB})\text{RhB}$  was confirmed to contain a  $\text{Rh} \equiv B$  quadruple bond.<sup>67</sup> The umbrella-like  $[(\eta^7\text{-B}_7)\text{-B-BO}]^-$  cluster was even found to embody metallomimetic properties of boron.<sup>68</sup>

Lead is one of the earliest metals acquainted and used by human beings. Despite their known toxicity, lead and its compounds are still important today and have wide applications in industries, including pigments, lead-acid batteries, and lead glasses, *etc.*<sup>69</sup> In fact, lead is the most common gamma-ray shielding material due to its high atomic number, high density, and wide availability.<sup>70–72</sup> Boron, on the other hand, has good shielding properties against neutron radiation because of its high thermal neutron absorption cross-section.<sup>73,74</sup> Recently, a series of lead borate crystals,  $\text{Pb}_3\text{B}_{10}\text{O}_{16}[\text{OH}]_4$ , have been synthesized and shown to have better co-shielding properties for gamma and neutron radiations than the simple  $\text{PbO/B}_2\text{O}_3$  mixture with the same molar ratio of Pb and B.<sup>75</sup> Despite the progress achieved for synthesizing lead borate compounds with various morphologies, few lead-boron molecules are known and our knowledge about the lead-boron bonding is still limited. We have studied recently two lead-doped boron oxide clusters,  $\text{PbB}_2\text{O}^{-/2-}$  and  $\text{PbB}_3\text{O}_2^-$  and found a  $\text{Pb} \equiv \text{B}$  triple bond in the linear  $\text{PbB}_2\text{O}^{2-}$  species, a  $\text{B} \equiv \text{Pb}$  multiple bond with a bond order of 2.5 in the linear  $\text{PbB}_2\text{O}^-$ , and a  $\text{B}=\text{Pb}$  double bond in the Y-shaped  $\text{PbB}_3\text{O}_2^-$ .<sup>76</sup>

In this article, we report the observation of three lead-doped boron and boron oxide clusters,  $\text{PbB}_2^-$ ,  $\text{PbB}_3\text{O}^-$ , and  $\text{PbB}_4\text{O}_2^-$ , which are studied *via* photoelectron spectroscopy (PES) and *ab initio* calculations. The global minimum (GM) of  $\text{PbB}_2^-$  is found to be an isosceles triangle, while the GM structures of  $\text{PbB}_3\text{O}^-$  and  $\text{PbB}_4\text{O}_2^-$  can be viewed as successively coordinating a boronyl ligand colinearly to the B atoms of the triangular  $\text{PbB}_2^-$ . The triangular  $\text{PbB}_2^-$  is aromatic and contains a  $\text{B}=\text{B}$  double bond and two  $\text{Pb}-\text{B}$  single bonds. The coordination of BO is observed to strengthen the  $\text{B}=\text{B}$  double bond in  $\text{PbB}_2^-$  but weaken  $\text{Pb}-\text{B}$  bonding. Thus, the GM structures of the three lead-doped boron clusters can be formulated as  $[\text{PbB}_2(\text{BO})_n]^-$  ( $n = 0-2$ ), with zero, one, and two boronyl units bonded to an aromatic  $\text{PbB}_2$  triangle. It is found that Pb bonding with the  $\text{B}_2$  part of the  $\text{B}_2(\text{BO})_2$  motif in  $[\text{PbB}_2(\text{BO})_2]^{-/0}$  is very weak and these entities can be characterized as the  $\text{Pb}^{+/2+}[\text{B}_2(\text{BO})_2]^{2-}$  charge-transfer complexes containing a  $\text{B} \equiv \text{B}$  triple bond. A low-lying Y-shaped isomer is also observed for  $\text{PbB}_4\text{O}_2^-$ , which consists of a central B atom in  $\text{sp}^2$  hybridization and coordinated by two boronyl ligands and a  $\text{B}=\text{B}$  double bond with the  $\text{PbB}$  unit  $[\text{PbB} = \text{B}(\text{B} \equiv \text{O})_2]^-$ . These findings not only broaden our understanding of  $\text{Pb}-\text{B}$  bonding but also help design novel lead-boron molecules and lead boride materials with excellent co-shielding properties for high-energy gamma and neutron radiations.

## 2 Method

### 2.1 Photoelectron spectroscopy

The lead-boron clusters were produced using a laser vaporization cluster source and were investigated using a magnetic-

bottle PES apparatus, as described previously.<sup>7,77</sup> Briefly, the  $\text{PbB}_2^-$ ,  $\text{PbB}_3\text{O}^-$ , and  $\text{PbB}_4\text{O}_2^-$  clusters were formed by laser vaporization of a cold-pressed  $\text{Pb}/^{10}\text{B}$  mixed target with a helium carrier seeded with 5% Ar, and the 532 nm vaporization laser beam was directed collinearly with the cluster beam. The trace amount of oxide impurities on the target surface was sufficient to produce the O-containing species,  $\text{PbB}_3\text{O}^-$  and  $\text{PbB}_4\text{O}_2^-$ . Seeding the helium carrier gas with  $\text{O}_2$  would produce highly oxidized clusters ( $\text{PbB}_x\text{O}_y^-$ ). The clusters formed in the source were entrained in the carrier gas pulse delivered by two symmetrically mounted molecular beam valves and underwent a supersonic expansion. We used a large waiting room nozzle and a strong supersonic expansion to remove the substantial internal energies to maximize cluster cooling. After passing a skimmer, negatively charged clusters were extracted from the collimated cluster beam and analyzed using a time-of-flight mass spectrometer. The clusters of current interest were mass-selected and decelerated before photodetached by a pulsed laser beam at 266 nm (4.661 eV) produced from the fourth harmonics of a Nd:YAG laser. Photoelectron kinetic energies were calibrated using the known spectrum of the  $\text{Bi}^-$  atomic anion. The resolution of the magnetic-bottle PES apparatus was around 2.5%, that is,  $\sim 25$  meV for 1 eV electrons.

### 2.2 Computational methods

The GM structures were searched for  $\text{PbB}_2^-$ ,  $\text{PbB}_3\text{O}^-$ , and  $\text{PbB}_4\text{O}_2^-$  using the Coalescence-Kick method<sup>78</sup> at the PBE0/lanl2dz<sup>79–82</sup> level of theory. Low-lying candidates were fully optimized at the PBE0 level with the augmented Dunning's all-electron basis set (aug-cc-pVTZ) for B and O atoms and the aug-cc-pVTZ-pp basis set with the relativistic pseudopotentials (ECP60MDF) for the Pb atom (abbreviated as AVTZ).<sup>83,84</sup> Vibrational frequencies were calculated at the same level to make sure that the obtained structures exhibited true minima of the systems. The relative energies of the top isomers within 1.0 eV were further refined at the CCSD(T)<sup>85–87</sup>/AVTZ//PBE0/AVTZ level [abbreviated as CCSD(T)/AVTZ]. To obtain more reliable structural parameters, we re-optimized the lowest-lying isomer for each species and the second lowest-lying isomer of  $\text{PbB}_4\text{O}_2^-$  at the CCSD/AVTZ level.<sup>88,89</sup> The first vertical detachment energies ( $\text{VDE}_1$ ) and the adiabatic detachment energies (ADE) for the GM structures of  $\text{PbB}_2^-$ ,  $\text{PbB}_3\text{O}^-$ , and  $\text{PbB}_4\text{O}_2^-$  were calculated at the CCSD(T)/AVTZ level. The  $\text{VDE}_1$  was computed as the energy difference between the anionic ground state and the corresponding neutral ground state at the optimized anion geometry, whereas the ADE was calculated as the difference in energy between the optimized anion and the corresponding neutral at its optimized structure.

The higher VDEs were obtained by adding the neutral excitation energies to the  $\text{VDE}_1$ . To obtain the energies of the neutral excited states, the state-averaged (SA) complete active space self-consistent field (CASSCF) calculations<sup>90,91</sup> were performed using the AVTZ basis set, followed by multi-reference configuration interaction (MRCI) calculations,<sup>92</sup> in which the spin-orbit (SO) coupling effect was considered.<sup>93</sup> The active space employed consisted of 8 electrons in 10 orbitals for  $\text{PbB}_2$ ,

5 electrons in 6 orbitals for  $\text{PbB}_3\text{O}$ , and 4 electrons in 6 orbitals for  $\text{PbB}_4\text{O}_2$ . For the second isomer of  $\text{PbB}_4\text{O}_2^-$ , the first two VDEs were calculated at the CCSD(T)/AVTZ level as the transition from the ground state of the anionic species to the lowest singlet and triplet states of the corresponding neutral species at the optimized anion geometry. The higher VDEs were calculated using the time-dependent (TD)-PBE0/AVTZ method. Vibrational frequencies for the ground state of neutral  $\text{PbB}_3\text{O}$  were computed at the PBE0/AVTZ level. Chemical bonding analyses were conducted using the adaptive natural density partitioning (AdNDP) method<sup>94</sup> and were then visualized using the VMD software.<sup>95</sup> The out-of-plane tensor components of the nucleus-independent chemical shift at  $\zeta$  distance above the molecular plane  $[\text{NICS}_{\text{zz}}(\zeta)]$ <sup>96</sup> were computed at the PBE0/TZP<sup>97</sup> level to examine the aromaticity of the experimentally confirmed species. Considering the influence of heavy metal doping on the aromaticity indices,<sup>98</sup> the centres of the ring currents were used instead of the geometry centres to calculate the  $\text{NICS}_{\text{zz}}(\zeta)$  values, and the spin-orbit coupling effects were included in the NICS calculations.<sup>99,100</sup> Natural bond orbital (NBO) and natural resonance theory (NRT) analyses<sup>101</sup> were performed at the PBE0/AVTZ level using the NBO 7.0 program.<sup>102</sup> All geometry optimizations and frequency calculations at the PBE0 and CCSD levels and TD-PBE0 calculations were performed using the Gaussian 09 program.<sup>103</sup> The CCSD(T), CASSCF, and MRCI calculations were carried out using the Molpro package.<sup>104</sup> The NICS calculations were implemented using the ADF code,<sup>105</sup> while the centres of the ring current were searched using the GIMIC program.<sup>106</sup>

### 3 Experimental results

The photoelectron spectra of  $\text{PbB}_2^-$ ,  $\text{PbB}_3\text{O}^-$ , and  $\text{PbB}_4\text{O}_2^-$  at 266 nm are shown in Fig. 1–3, respectively. The well-resolved PES bands are labeled with letters, X, A, B, ..., where band X represents the transition from the anionic ground state to the electronic ground state of the corresponding neutral cluster and bands A, B, ... indicate detachment transitions to the excited electronic states of the neutral cluster. The electron affinity (EA) of the corresponding neutral cluster or the ADE

was determined by drawing a straight line at the leading edge of band X and then adding the instrumental resolution. The VDEs were measured using the band maxima, as given in Tables 1–3, where they are compared with the theoretical results. A larger difference between the  $\text{VDE}_1$  and ADE usually indicates a more significant geometry change from the anion to neutral cluster upon electron detachment.

#### 3.1 $\text{PbB}_2^-$

The 266 nm spectrum of  $\text{PbB}_2^-$  shown in Fig. 1 displays six sharp and intense peaks on the low binding energy side and weak and broader PES features above 3.5 eV. The first VDE of  $\text{PbB}_2^-$  is obtained from band X as 2.08 eV and the ADE is estimated to be 2.03 eV, which also represents the EA of  $\text{PbB}_2$ . An intense band A is observed at 2.48 eV, followed by a similarly intense band B at 2.65 eV. Three closely spaced bands C, D, E are observed at 2.91, 3.03, and 3.15 eV, respectively. Features beyond 3.5 eV are weak and congested, and they are labeled as F for the sake of discussion. All the VDEs for  $\text{PbB}_2^-$  are given in Table 1 and compared with the theoretical data.

#### 3.2 $\text{PbB}_3\text{O}^-$

The 266 nm spectrum of  $\text{PbB}_3\text{O}^-$  (Fig. 2) is relatively simple with three sharp and well-resolved bands. Band X gives rise to the first VDE at 3.10 eV, with its ADE estimated as 3.08 eV, followed by band A at 3.32 eV.  $\text{PbB}_3\text{O}^-$  has the highest VDE among all three clusters due to its closed-shell electronic structure. Band B at 3.85 eV was vibrationally resolved with a vibrational spacing of  $\sim 480\text{ cm}^{-1}$ . A very weak feature marked by an asterisk was observed at the low binding energy side, which might come from a contaminant due to the congested mass spectrum caused by the isotopic distribution of lead. The measured VDEs for  $\text{PbB}_3\text{O}^-$  are summarized in Table 2, where they are compared with the theoretical results.

#### 3.3 $\text{PbB}_4\text{O}_2^-$

The photoelectron spectrum of  $\text{PbB}_4\text{O}_2^-$  (Fig. 3) seems much more complicated than those for  $\text{PbB}_2^-$  and  $\text{PbB}_3\text{O}^-$  with more congested features. The PES bands labeled with X, A–E are intense and relatively sharp, which are likely from one species. On the other hand, the two bands labeled with X' (3.13 eV) and A' (3.40 eV) are weak and broad and they appear to come from a minor isomer of  $\text{PbB}_4\text{O}_2^-$ . Band X yields a VDE of 2.88 eV with an estimated ADE of 2.84 eV. Following a relatively large energy gap of 1 eV, a sharp and intense band A is observed at 3.82 eV. The spectral features beyond band A become more complex, and a weaker peak B is observed at 4.01 eV, while a relatively broad band C is resolved at 4.15 eV. Two sharp bands, D and E, are observed at 4.33 and 4.53 eV, respectively. The bands C, D, and E appear to contain partially resolved vibrational features. The VDEs for band X, A–E are given in Table 3 and compared with the theoretical results to be presented below.

### 4 Theoretical results

Fig. 4 displays the optimized GM structures and their bond lengths of  $\text{PbB}_2^-$  and  $\text{PbB}_3\text{O}^-$  and the top two lowest-lying

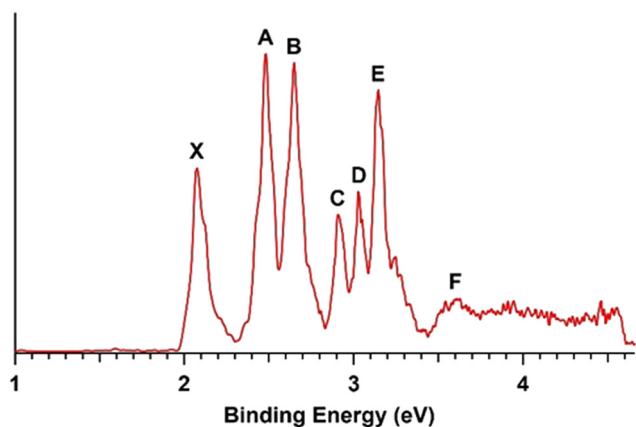


Fig. 1 Photoelectron spectrum of  $\text{PbB}_2^-$  at 266 nm (4.661 eV).

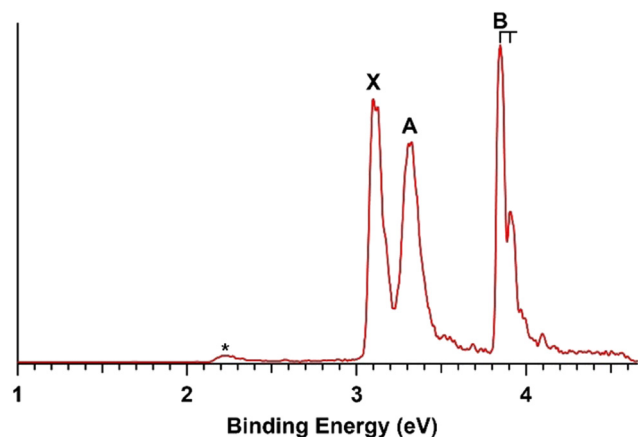


Fig. 2 Photoelectron spectrum of  $\text{PbB}_2\text{O}^-$  at 266 nm.

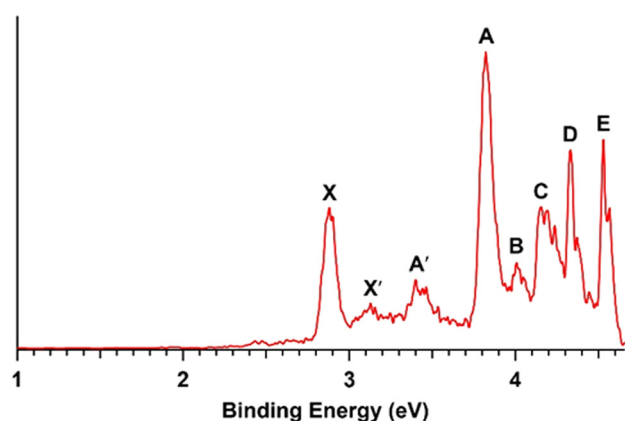


Fig. 3 Photoelectron spectrum of  $\text{PbB}_4\text{O}_2^-$  at 266 nm.

isomers of  $\text{PbB}_4\text{O}_2^-$  at the CCSD/AVTZ level. All low-lying structures within about 2.0 eV of the GM structure at the PBE0/AVTZ level are presented in Fig. S1–S3 (ESI†) for  $\text{PbB}_2^-$ ,  $\text{PbB}_3\text{O}^-$ , and  $\text{PbB}_4\text{O}_2^-$ , respectively, along with their symmetries, electronic states, and relative energies. The top isomers within 1.0 eV were further calculated at the single-point CCSD(T)/AVTZ level.

#### 4.1 $\text{PbB}_2^-$

Only six structures with different spin multiplicities (doublet, quartet, and sextet) are located within  $\sim 2.0$  eV of the GM for the  $\text{PbB}_2^-$  cluster (Fig. S1, ESI†). These structures can be divided into two categories, *i.e.*,  $C_{2v}$  isosceles triangle and linear Pb–B–B. It is found that the doublet isosceles triangle ( $C_{2v}$ ,  $^2A_1$ ) is the GM for  $\text{PbB}_2^-$ , consisting of a  $\text{B}_2$  dimer bridged by a Pb atom (Fig. 4, 1). The second lowest-lying isomer, a doublet linear Pb–B–B ( $C_{\infty v}$ ,  $^2\Sigma$ ) structure, is more than 0.45 eV above the GM at both the PBE0 and CCSD(T) levels. The remaining isomers are at least 1.11 eV higher in energy at the PBE0 level.

#### 4.2 $\text{PbB}_3\text{O}^-$

Candidate structures for  $\text{PbB}_3\text{O}^-$  are composed of five isomers containing a terminal BO group bonded to a  $\text{PbB}_2$  moiety and another five isomers based on a  $\text{B}_3$  triangle (Fig. S2, ESI†). The GM of  $\text{PbB}_3\text{O}^-$  is 2 ( $C_s$ ,  $^1A'$ ), as shown in Fig. 4 with all bond lengths labeled. The GM can be viewed as attaching a BO group to a B atom of the  $\text{PbB}_2$  triangle along the B–B bond, weakening the Pb–B bond while strengthening the terminal Pb–B bond. The closest low-lying isomer consists of a  $\text{B}_3$  triangle with a bridging Pb atom and a bridging O atom, which is 0.84 eV higher in energy than the GM at the PBE0 level and 1.00 eV higher at the CCSD(T) level. The large energy gap between the first two isomers indicates the high stability of GM 2.

#### 4.3 $\text{PbB}_4\text{O}_2^-$

For the  $\text{PbB}_4\text{O}_2^-$  cluster, we found fourteen isomers within 2 eV of the GM, most of which possess at least one terminal BO group (Fig. S3, ESI†). The GM of  $\text{PbB}_4\text{O}_2^-$  (3  $C_{2v}$ ,  $^2B_2$ ) is a planar structure, consisting of two terminal BO groups and a  $\text{PbB}_2$  isosceles triangle (Fig. 4). It can be viewed as attaching a BO unit to each of the two B atoms of the GM of  $\text{PbB}_2^-$  (1) colinearly, significantly weakening the B–Pb bonds while strengthening the B–B bonds of the  $\text{PbB}_2$  unit. The second lowest-lying isomer (4  $C_{2v}$ ,  $^2B_2$ ) is less stable than the GM by  $\sim 0.95$  eV at both the PBE0 and CCSD(T) levels (Fig. S3, ESI†). It has a Y-shaped structure (Fig. 4), similar to the recently reported

**Table 1** The experimental VDEs for  $\text{PbB}_2^-$ , and their assignments and comparison with the theoretical results. All energies are given in eV. The first VDE was calculated using the CCSD(T) method. MRCI and SO coupling calculations were conducted to calculate the higher VDEs

VDE (Exp) <sup>a</sup>		Configurations	Terms	VDE (MRCI)	Levels	VDE (SO)	Composition of SO coupled states
X	2.08	$1a_1^2 2a_1^2 1b_2^2 3a_1^2 1b_1^2 4a_1^0$	$^1A_1$	1.94	$^1A_{1(0)}$	1.94	$96.4\%^1A_1 + 3.3\%^3B_2 + 0.3\%^3B_1$
A	2.48	$1a_1^2 2a_1^2 1b_2^2 3a_1^1 1b_1^2 4a_1^1$	$^3A_1$	2.54	$^3A_{1(0)}$	2.52	$65.2\%^3A_1 + 34.8\%^3B_1$
					$^3A_{1(-1)}$	2.52	$63.8\%^3A_1 + 36.2\%^3B_1$
B	2.65	$1a_1^2 2a_1^2 1b_2^2 3a_1^2 1b_1^1 4a_1^1$	$^3B_1$	2.65	$^3A_{1(+1)}$	2.61	$94.8\%^3A_1 + 3.6\%^1B_1 + 1.6\%^3B_2$
					$^3B_{1(+1)}$	2.69	$87.0\%^3B_1 + 12.5\%^1A_1 + 0.4\%^3B_2$
C	2.91				$^3B_{1(-1)}$	2.86	$62.2\%^3B_1 + 31.7\%^3A_1 + 6.1\%^1B_2$
					$^3B_{1(0)}$	2.90	$63.6\%^3B_1 + 36.0\%^3A_1 + 0.4\%^1B_2$
D	3.03	$1a_1^2 2a_1^2 1b_2^2 3a_1^1 1b_1^2 4a_1^1$	$^1A_1$	3.00	$^1A_{1(0)}$	3.11	$68.6\%^1A_1 + 23.0\%^3B_2 + 8.4\%^3B_1$
E	3.15	$1a_1^2 2a_1^2 1b_2^2 3a_1^2 1b_1^1 4a_1^1$	$^1B_1$	3.09	$^1B_{1(0)}$	3.25	$81.0\%^1B_1 + 17.0\%^3B_2 + 2.0\%^3A_1$
F	$\sim 3.6$	$1a_1^2 2a_1^2 1b_2^2 3a_1^2 1b_1^2 4a_1^1$	$^3B_2$	3.85	$^3B_{2(0)}$	4.06	$96.4\%^3B_2 + 1.9\%^3A_1 + 1.7\%^1B_1$
					$^3B_{2(+1)}$	4.06	$97.0\%^3B_2 + 1.9\%^3A_1 + 1.1\%^1B_1$
					$^3B_{2(-1)}$	4.08	$96.7\%^3B_2 + 2.4\%^1A_1 + 0.9\%^3B_1$

<sup>a</sup> The experimental uncertainty was estimated to be  $\pm 0.02$  eV.



**Table 2** The experimental VDEs for  $\text{PbB}_3\text{O}^-$ , their assignments and comparison with the theoretical results. All energies are given in eV. The first VDE was calculated using the CCSD(T) method. MRCI and SO coupling calculations were conducted to calculate higher VDEs

VDE (exp.) <sup>a</sup>	Configurations	Terms	VDE (MRCI)	Levels	VDE (SO)	Composition of SO coupled states
X 3.10	...5a' <sup>2</sup> 6a' <sup>2</sup> 1a'' <sup>2</sup> 7a' <sup>2</sup> 8a' <sup>2</sup> 2a'' <sup>1</sup>	<sup>2</sup> A''	3.21	<sup>2</sup> A'' <sub>±1/2</sub>	3.21	70.1% <sup>2</sup> A'' + 26.1% <sup>2</sup> A' + 2.1% <sup>4</sup> A' + 1.7% <sup>4</sup> A''
A 3.32	...5a' <sup>2</sup> 6a' <sup>2</sup> 1a'' <sup>2</sup> 7a' <sup>1</sup> 8a' <sup>2</sup> 2a'' <sup>2</sup>	<sup>2</sup> A'	3.23	<sup>2</sup> A' <sub>±1/2</sub>	3.48	80.4% <sup>2</sup> A' + 15.9% <sup>2</sup> A'' + 1.6% <sup>4</sup> A' + 2.1% <sup>4</sup> A''
B 3.85	...5a' <sup>2</sup> 6a' <sup>2</sup> 1a'' <sup>2</sup> 7a' <sup>2</sup> 8a' <sup>1</sup> 2a'' <sup>2</sup>	<sup>2</sup> A'	3.66	<sup>2</sup> A' <sub>±1/2</sub>	3.96	84.2% <sup>2</sup> A' + 9.6% <sup>2</sup> A'' + 3.3% <sup>4</sup> A' + 2.9% <sup>4</sup> A''

<sup>a</sup> The experimental uncertainty was estimated to be ±0.02 eV.

**Table 3** The experimental VDEs for  $\text{PbB}_4\text{O}_2^-$ , their assignments and comparison with the theoretical results. All energies are given in eV. The first VDE was calculated using the CCSD(T) method. MRCI and SO coupling calculations were conducted to calculate higher VDEs

VDE (exp.) <sup>a</sup>	Configurations	Terms	VDE (MRCI)	Levels	VDE (SO)	Composition of SO coupled states
X 2.88	...1b <sub>1</sub> <sup>2</sup> 1a <sub>2</sub> <sup>2</sup> 4b <sub>2</sub> <sup>2</sup> 6a <sub>1</sub> <sup>2</sup> 2b <sub>1</sub> <sup>2</sup> 7a <sub>1</sub> <sup>2</sup> 5b <sub>2</sub> <sup>0</sup>	<sup>1</sup> A <sub>1</sub>	2.88	<sup>1</sup> A <sub>1(0)</sub>	2.88	85.0% <sup>1</sup> A <sub>1</sub> + 9.6% <sup>3</sup> B <sub>2</sub> + 2.8% <sup>3</sup> A <sub>2</sub> + 2.5% <sup>3</sup> B <sub>1</sub>
A 3.82	...1b <sub>1</sub> <sup>2</sup> 1a <sub>2</sub> <sup>2</sup> 4b <sub>2</sub> <sup>2</sup> 6a <sub>1</sub> <sup>2</sup> 2b <sub>1</sub> <sup>2</sup> 7a <sub>1</sub> <sup>1</sup> 5b <sub>2</sub> <sup>1</sup>	<sup>3</sup> B <sub>2</sub>	3.85	<sup>3</sup> B <sub>2(0)</sub>	3.86	59.0% <sup>3</sup> B <sub>2</sub> + 36.3% <sup>3</sup> A <sub>2</sub> + 2.3% <sup>3</sup> A <sub>1</sub> + 2.4% <sup>1</sup> B <sub>1</sub>
				<sup>3</sup> B <sub>2(-1)</sub>	3.86	51.8% <sup>3</sup> B <sub>2</sub> + 41.3% <sup>3</sup> A <sub>2</sub> + 4.6% <sup>1</sup> A <sub>1</sub> + 2.2% <sup>3</sup> B <sub>1</sub>
				<sup>3</sup> B <sub>2(+1)</sub>	3.91	82.8% <sup>3</sup> B <sub>2</sub> + 12.9% <sup>1</sup> A <sub>2</sub> + 3.2% <sup>3</sup> B <sub>1</sub> + 1.1% <sup>3</sup> A <sub>1</sub>
B 4.01	...1b <sub>1</sub> <sup>2</sup> 1a <sub>2</sub> <sup>2</sup> 4b <sub>2</sub> <sup>2</sup> 6a <sub>1</sub> <sup>2</sup> 2b <sub>1</sub> <sup>1</sup> 7a <sub>1</sub> <sup>1</sup> 5b <sub>2</sub> <sup>1</sup>	<sup>3</sup> A <sub>2</sub>	3.96	<sup>3</sup> A <sub>2(+1)</sub>	4.03	89.6% <sup>3</sup> A <sub>2</sub> + 6.9% <sup>3</sup> A <sub>1</sub> + 3.4% <sup>1</sup> B <sub>2</sub> + 0.1% <sup>3</sup> B <sub>1</sub>
C 4.15				<sup>3</sup> A <sub>2(-1)</sub>	4.15	56.1% <sup>3</sup> A <sub>2</sub> + 38.0% <sup>3</sup> B <sub>2</sub> + 4.7% <sup>3</sup> A <sub>1</sub> + 1.3% <sup>1</sup> B <sub>1</sub>
D 4.33	...1b <sub>1</sub> <sup>2</sup> 1a <sub>2</sub> <sup>2</sup> 4b <sub>2</sub> <sup>2</sup> 6a <sub>1</sub> <sup>2</sup> 2b <sub>1</sub> <sup>1</sup> 7a <sub>1</sub> <sup>1</sup> 5b <sub>2</sub> <sup>1</sup>	<sup>1</sup> A <sub>2</sub>	4.19	<sup>3</sup> A <sub>2(0)</sub>	4.38	54.4% <sup>3</sup> A <sub>2</sub> + 34.0% <sup>3</sup> B <sub>2</sub> + 11.6% <sup>1</sup> A <sub>1</sub>
				<sup>1</sup> A <sub>2(0)</sub>	4.34	76.2% <sup>1</sup> A <sub>2</sub> + 12.9% <sup>3</sup> B <sub>2</sub> + 9.7% <sup>3</sup> A <sub>1</sub> + 1.3% <sup>3</sup> B <sub>1</sub>
E 4.53	...1b <sub>1</sub> <sup>2</sup> 1a <sub>2</sub> <sup>2</sup> 4b <sub>2</sub> <sup>2</sup> 6a <sub>1</sub> <sup>2</sup> 2b <sub>1</sub> <sup>2</sup> 7a <sub>1</sub> <sup>1</sup> 5b <sub>2</sub> <sup>1</sup>	<sup>1</sup> B <sub>2</sub>	4.56	<sup>1</sup> B <sub>2(0)</sub>	4.70	81.9% <sup>1</sup> B <sub>2</sub> + 14.6% <sup>3</sup> B <sub>1</sub> + 3.4% <sup>3</sup> A <sub>2</sub>

<sup>a</sup> The experimental uncertainty was estimated to be ±0.02 eV.

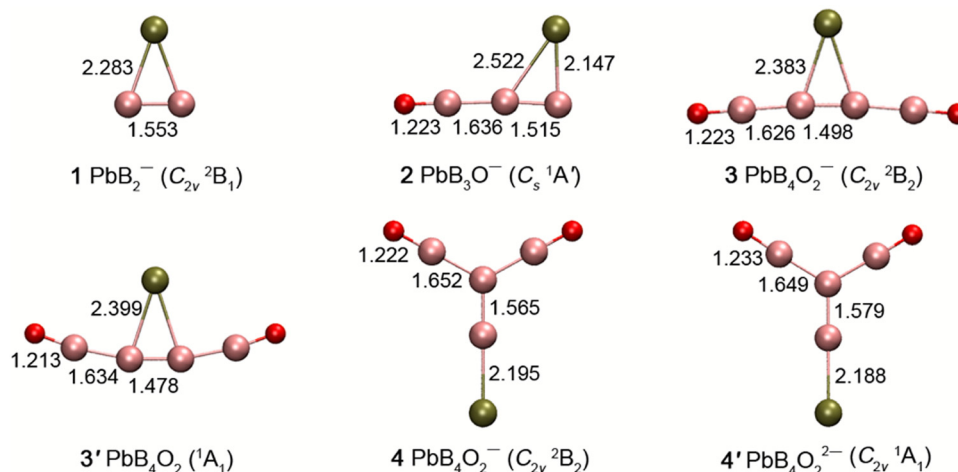


**Fig. 4** The optimized structures of the GM of  $\text{PbB}_2^-$  (**1**),  $\text{PbB}_3\text{O}^-$  (**2**),  $\text{PbB}_4\text{O}_2^-$  (**3**) and its closed-shell  $\text{PbB}_4\text{O}_2$  (**3'**), and a low-lying isomer of  $\text{PbB}_4\text{O}_2^-$  (**4**) and its closed-shell  $\text{PbB}_4\text{O}_2^{2-}$  (**4'**). The bond lengths are given in Å at the CCSD/AVTZ level.

$\text{C}_{2v}$   $\text{PbB}_3\text{O}_2^-$ ,<sup>76</sup> and can be viewed as two boronyl groups and one Pb–B unit coordinated to a central B atom. Overall, the GM structures of  $\text{PbB}_2^-$  (**1**),  $\text{PbB}_3\text{O}^-$  (**2**), and  $\text{PbB}_4\text{O}_2^-$  (**3**) can be expressed as  $[\text{PbB}_2(\text{BO})_n]^-$  ( $n = 0-2$ ), *i.e.*, zero, one, and two boronyl ligands coordinated to a triangular  $\text{PbB}_2$  core.

## 5 Discussion

### 5.1 Comparison between experiment and theory

The predicted VDEs are summarized in Tables 1–3 for the GM structures of  $\text{PbB}_2^-$ ,  $\text{PbB}_3\text{O}^-$ , and  $\text{PbB}_4\text{O}_2^-$ , respectively, in

comparison with the experimentally measured values, as well as in Fig. 5–7. The computed ADE/VDE<sub>1</sub> values for the GM structures of  $\text{PbB}_2(\text{BO})_n$  ( $n = 0-2$ ) and the VDE<sub>1</sub> for the low-lying isomer of  $\text{PbB}_4\text{O}_2^-$  are compared with the experimental results in Table 4. The theoretical VDEs were calculated using the CCSD(T) method for VDE<sub>1</sub> and using the SA-CASSCF method for higher VDEs. The valence molecular orbitals (MOs) of the GM structures of  $\text{PbB}_2^-$ ,  $\text{PbB}_3\text{O}^-$ , and  $\text{PbB}_4\text{O}_2^-$  are depicted in Fig. S4 (ESI†).

**5.1.1. PbB<sub>2</sub><sup>-</sup>.** For the C<sub>2v</sub> GM of  $\text{PbB}_2^-$  (**1**), detachment of the electron from the 4a<sub>1</sub> SOMO (Fig. S4a, ESI†) leads to the singlet <sup>1</sup>A<sub>1</sub> ground state of neutral  $\text{PbB}_2\text{O}$  (Table 1). The calculated ADE of

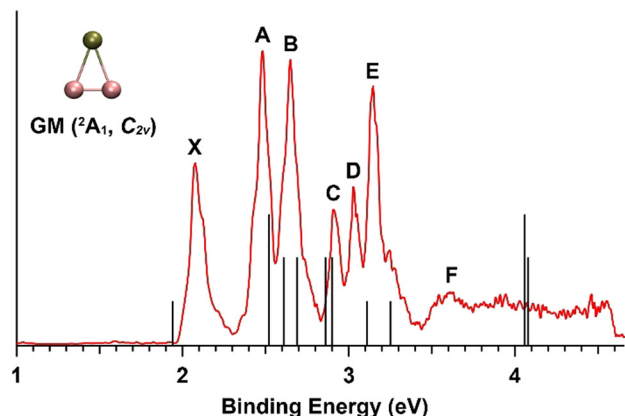


Fig. 5 Comparison of the photoelectron spectrum of  $\text{PbB}_2^-$  with the computed VDEs. The vertical bars correspond to the computed VDEs using the CCSD(T) + SA-CASSCF method. The shortest bars correspond to singlet final states and the slightly longer bars correspond to triplet final states, and the longest bars indicate degenerate states at the same energy.

1.91 eV and  $\text{VDE}_1$  of 1.94 eV at the CCSD(T) level agree well with the experimental values at 2.03 eV and 2.08 eV, respectively (Table 4). The next two detachment channels are derived from the removal of the  $\beta$  electron from the  $3a_1$  HOMO-2 and the  $1b_1$  HOMO-1, resulting in the triplet  $^3A_1$  and  $^3B_1$  final states, respectively (Table 1). The  $^3A_1$  state splits into three closely-spaced SO states  $^3A_{1(0)}$ ,  $^3A_{1(-1)}$ , and  $^3A_{1(+1)}$  with predicted VDEs of 2.52, 2.52, and 2.61 eV, while the  $^3B_1$  state also gives rise to three SO states  $^3B_{1(+1)}$ ,  $^3B_{1(-1)}$ , and  $^3B_{1(0)}$  with computed VDEs of 2.69, 2.86, and 2.90 eV, respectively (Table 1). These SO states should account for the observed PES bands A (2.48 eV), B (2.65 eV), and C (2.91 eV). The next two singlet final states  $^1A_1$  and  $^1B_1$  with the calculated VDEs of 3.11 and 3.25 eV are derived by removing the  $\alpha$  electron from the HOMO-2 ( $3a_1$ ) and the HOMO-1 ( $1b_1$ ), in good agreement with the observed bands D and E at 3.03 and 3.15 eV, respectively. Detachment of the  $\beta$  electron from the deeper HOMO-3 ( $1b_2$ ) results in the triplet  $^3B_2$  final state, which gives rise to three SO-split final states,  $^3B_{2(0)}$ ,  $^3B_{2(+1)}$ , and  $^3B_{2(-1)}$ . These final states along with detachment from even deeper MOs should account for the congested PES signals beyond 3.5 eV. Overall, the theoretical VDEs for  $\text{PbB}_2^-$  with the SO effects are in good agreement with the experimental data (Fig. 5), confirming triangular structure **1** as the GM of  $\text{PbB}_2^-$ .

**5.1.2.  $\text{PbB}_3\text{O}^-$ .** The  $C_s$  GM of  $\text{PbB}_3\text{O}^-$  (**2**) possesses a closed-shell electronic configuration with a  $^1A'$  ground state and thus only doublet final states are expected upon one-electron detachment. The first detachment channel corresponds to the removal of an electron from the HOMO ( $2a''$ ) (Fig. S4b, ESI†), giving rise to a  $^2A''$  neutral ground state (Table 2). The calculated ADE/ $\text{VDE}_1$  values are 3.16/3.21 eV at the CCSD(T) level (Table 4), in reasonable agreement with experimental values of 3.08/3.10 eV. Following a small energy gap of 0.27 eV, the second and third VDEs are predicted to be 3.48 eV and 3.96 eV (Table 2), resulting from electron detachment from the HOMO-2 ( $7a'$ ) and the HOMO-1 ( $8a'$ ), respectively. These two VDEs, separated by 0.48 eV, are consistent with observed bands A (3.32 eV) and B (3.85 eV). The energy intervals of these three detachment channels can well

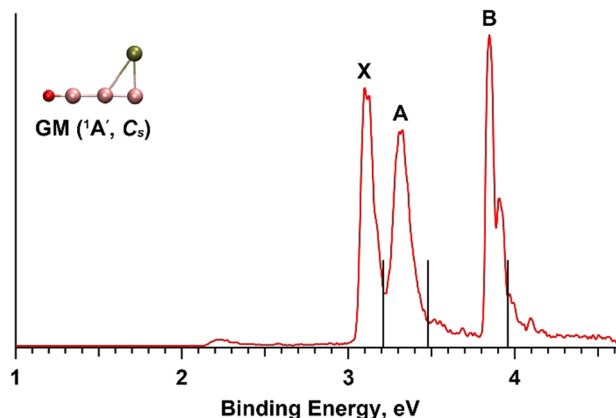


Fig. 6 Comparison of the photoelectron spectrum with the computed VDEs for the GM of  $\text{PbB}_3\text{O}^-$ . The vertical bars correspond to the computed VDEs using the CCSD(T) + SA-CASSCF method.

reproduce the observed energy gaps between bands X and A (0.22 eV) and between bands A and B (0.53 eV), as shown in Table 2 and Fig. 6. The observed vibrational structures with a

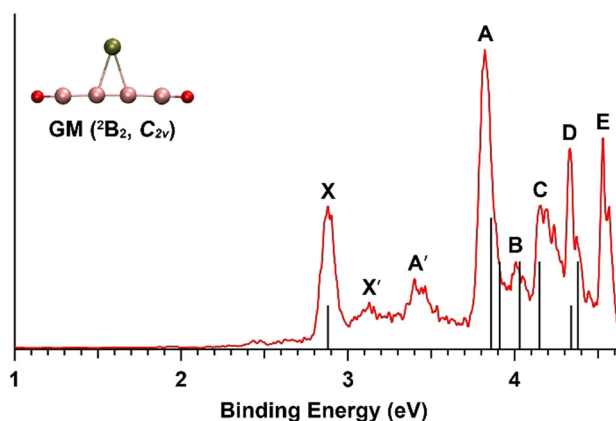


Fig. 7 Comparison of the photoelectron spectrum with the computed VDEs for the  $C_{2v}$  GM of  $\text{PbB}_4\text{O}_2^-$ . The vertical bars correspond to the computed VDEs using the CCSD(T) + SA-CASSCF method. The shortest bars correspond to singlet final states and the slightly longer bars correspond to triplet final states, and the longest bars indicate degenerate states at the same energy. Note that the detachment channel corresponding to band E has a computed VDE of 4.70 eV (Table 3), slightly out of the scale of the figure. The PES bands X' and A' are due to isomer **4** (see Fig. S5, ESI†).

Table 4 Comparison of the experimental ADE and  $\text{VDE}_1$  with calculated values for the GM of  $\text{PbB}_2(\text{BO})_n^-$  ( $n = 0-2$ ) and a low-lying isomer for  $n = 2$  at the PBE0/AVTZ and CCSD(T)/AVTZ levels. All energies are given in eV

Species	final state	ADE (theo.)		$\text{VDE}_1$ (theo.)		ADE (exp) <sup>a</sup>	$\text{VDE}_1$ (exp) <sup>a</sup>
		PBE0	CCSD(T)	PBE0	CCSD(T)		
$\text{PbB}_2^-$ $C_{2v}$ ( <b>1</b> )	$^1A_1$	2.26	1.91	2.29	1.94	2.03	2.08
$\text{PbB}_3\text{O}^-$ , $C_s$ ( <b>2</b> )	$^2A''$	3.10	3.16	3.18	3.21	3.08	3.10
$\text{PbB}_4\text{O}_2^-$ , $C_{2v}$ ( <b>3</b> )	$^1A_1$	2.86	2.75	3.01	2.88	2.84	2.88
	$C_{2v}$ ( <b>4</b> ) $^1A_1$	3.27	3.16	3.29	3.16		3.13 <sup>b</sup>

<sup>a</sup> The experimental uncertainty was estimated to be  $\pm 0.02$  eV. <sup>b</sup> Measured from the observed weak band X' in Fig. 3.

spacing of  $\sim 480\text{ cm}^{-1}$  in band B are consistent with the calculated frequency for the terminal Pb–B stretching mode at  $533\text{ cm}^{-1}$ . The good agreement between the theoretical and experimental results lends considerable credence to the predicted GM of  $\text{PbB}_3\text{O}^-$  (2).

**5.1.3.  $\text{PbB}_4\text{O}_2^-$ .** The calculated  $\text{VDE}_1$  for the  $C_{2v}$  GM of  $\text{PbB}_4\text{O}_2^-$  (3) at the CCSD(T) level is 2.88 eV due to the electron detachment of the  $5b_2$  SOMO (Fig. S4c, ESI<sup>†</sup>), in excellent agreement with the observed band X at 2.88 eV. The ground state ADE is predicted as 2.75 eV at the CCSD(T) level, compared to the experimental value of 2.84 eV (Table 4). Detachment of the  $\beta$  electron from the HOMO-1 ( $7a_1$ ) gives rise to the triplet  $^3B_2$  final state, which results in three SO states  $^3B_{2(0)}$ ,  $^3B_{2(-1)}$ , and  $^3B_{2(+1)}$  with calculated VDEs of 3.86, 3.86, and 3.91 eV, respectively, in agreement with the observed intense band A at 3.82 eV (Table 3). The removal of one electron from the  $2b_1$  HOMO-2 can produce a triplet  $^3A_2$  state and a singlet  $^1A_2$  final state. The  $^3A_2$  state splits into three SO states  $^3A_{2(1)}$ ,  $^3A_{2(-1)}$ , and  $^3A_{2(0)}$  with calculated VDEs of 4.03, 4.15, and 4.38 eV, respectively. The singlet  $^1A_2$  final state yields a calculated VDE of 4.34 eV. The SO states  $^3A_{2(1)}$  and  $^3A_{2(-1)}$  agree well with the PES bands B and C at 4.01 and 4.15 eV, respectively, whereas the SO state  $^3A_{2(0)}$  and the singlet  $^1A_2$  state have similar VDEs, in agreement with band D at 4.33 eV. The next detachment channel with a calculated VDE of 4.70 eV corresponds to the  $^1B_2$  singlet final state due to the detachment of the  $\alpha$  electron from the  $7a_1$  HOMO-1, in good agreement with the observed band E at 4.53 eV.

It should be noted that the calculated VDEs for the  $C_{2v}$  GM of  $\text{PbB}_4\text{O}_2^-$  (3) cannot interpret the observed minor bands X' at 3.13 eV and A' at 3.40 eV. However, the first two detachment channels of the second isomer, the Y-shaped  $C_{2v}$   $\text{PbB}_4\text{O}_2^-$  (4), with the calculated VDEs of 3.16 and 3.45 eV (Table S1 and Fig. S5, ESI<sup>†</sup>), respectively, reproduce well the experimental VDEs of bands X' and A'. Moreover, the next two detachment channels (3.71 and 4.52 eV) of 4 may contribute weakly to bands A and E at 3.82 and 4.53 eV, respectively (Table S1 and Fig. S5, ESI<sup>†</sup>). The Y-shaped isomer 4 is 0.95 eV higher in energy than the GM structure 3 at the CCSD(T) level (Fig. S3, ESI<sup>†</sup>). Thus, it was surprising that Y-shaped isomer 4 was present in the experiment at all. There is likely a large kinetic barrier between the two structures, providing dynamic stability for 4 relative to GM 3. Overall, the excellent agreement between the theoretical and experimental data provides considerable credence to the identified GM of  $\text{PbB}_4\text{O}_2^-$  (3) and the existence of the low-lying isomer 4.

## 5.2 Aromaticity in $[\text{PbB}_2(\text{BO})_n]^-$ ( $n = 0-2$ )

The GM structures of the three Pb/B clusters can be viewed as starting from a triangular  $\text{PbB}_2^-$  unit with successive addition of a boronyl unit in  $\text{PbB}_3\text{O}^-$  [ $\text{PbB}_2(\text{BO})^-$ ] and  $\text{PbB}_4\text{O}_2^-$  [ $\text{PbB}_2(\text{BO})_2^-$ ]. These structural features again confirm the previous finding that the boronyl unit, isoelectronic to  $\text{CN}$ ,<sup>50</sup> is a strong ligand.<sup>51,53,56-68</sup> To understand the intrinsic nature of the high stability of the experimentally observed  $[\text{PbB}_2(\text{BO})_n]^-$  ( $n = 0-2$ ) clusters, we analyzed the chemical bonding for the GM structures of  $\text{PbB}_2^-$  (1) and  $\text{PbB}_3\text{O}^-$  (2), as well as that of  $\text{PbB}_4\text{O}_2^-$  (3) and its corresponding neutral  $\text{PbB}_4\text{O}_2$  (3', Fig. 4) using the AdNDP method, as

shown in Fig. 8. The AdNDP bonding analyses for the low-lying Y-shaped  $C_{2v}$   $\text{PbB}_4\text{O}_2^-$  (4) is presented in Fig. 9.

The AdNDP bonding analysis revealed that the  $C_{2v}$  GM of  $\text{PbB}_2^-$  (1) possesses one Pb 6s lone pair, one 2c-1e B–B  $\sigma$  bond, two 2c-2e Pb–B  $\sigma$  bonds, one delocalized 3c-2e Pb–B–B  $\sigma$  bond, and one delocalized 3c-2e Pb–B–B  $\pi$  bond (Fig. 8a). Due to the strong relativistic effects,<sup>107</sup> the 6s orbital is significantly stabilized and acts like a lone pair with little 6s-6p hybridization, similar to that found in Bi–B clusters.<sup>66,108</sup> The Pb–B bonding is basically obtained through the 6p orbitals of Pb and the sp orbitals of B. The  $\text{PbB}_2^-$  cluster exhibits  $\sigma + \pi$  double aromaticity with two  $\sigma$  and two  $\pi$  delocalized electrons fulfilling the  $4N + 2$  Hückel rule for each system. When boronyl units are successively added to  $\text{PbB}_2^-$  to produce  $\text{PbB}_3\text{O}^-$  [ $\text{PbB}_2(\text{BO})^-$ ] and  $\text{PbB}_4\text{O}_2^-$  [ $\text{PbB}_2(\text{BO})_2^-$ ], the B–B  $\sigma$  bond in  $\text{PbB}_2^-$  is consumed to form new B–BO  $\sigma$  bonds, while the two localized Pb–B  $\sigma$  bonds are transformed to two delocalized Pb–B<sub>2</sub>  $\sigma$  bonds. As shown in Fig. 8b, the  $C_s$  GM structure of  $\text{PbB}_3\text{O}^-$  (2) displays one Pb 6s lone pair, one 2c-2e B–BO  $\sigma$  bond, and a terminal  $\text{B}\equiv\text{O}$  group (one 1c-2e O lone pair, the  $\text{B}\equiv\text{O}$  triple bond: one 2c-2e B–O  $\sigma$  bond, and two 2c-2e B–O  $\pi$  bonds). The bonding between Pb and B<sub>2</sub> in 2 consists of three delocalized  $\sigma$  bonds and one delocalized  $\pi$  bond. Thus, the closed-shell  $C_s$   $\text{PbB}_3\text{O}^-$  (2) is doubly aromatic with six  $\sigma$  and two  $\pi$  delocalized electrons.

The AdNDP analysis for the  $C_{2v}$  GM structure of  $\text{PbB}_4\text{O}_2^-$  (3) readily identified the Pb 6s lone pair, two 2c-2e B–BO  $\sigma$  bonds, and two terminal  $\text{B}\equiv\text{O}$  triple bonds (Fig. 8c). The remaining valence electrons in the open-shell 3 consist of one 3c-1e  $\sigma$  bond, two 3c-2e  $\sigma$  bonds, and one 3c-2e delocalized  $\pi$  bond over the triangular  $\text{PbB}_2$  core, giving rise to five delocalized  $\sigma$  electrons and two delocalized  $\pi$  electrons. When the unpaired electron of 3 is detached to form the closed-shell neutral  $C_{2v}$   $\text{PbB}_4\text{O}_2$  (3'), the singly occupied 3c-1e  $\sigma$  bond is removed, and one of the delocalized 3c-2e  $\sigma$  bonds is transformed to the localized 2c-2e B–B bond. The closed-shell 3', thus, possesses one delocalized 3c-2e  $\sigma$  bond and one delocalized 3c-2e  $\pi$  bond on its  $\text{PbB}_2$  unit (Fig. 8d), making it  $\sigma + \pi$  doubly aromatic with two  $\sigma$  and two  $\pi$  delocalized electrons.

To quantitatively assess the double aromatic character of  $C_{2v}$   $\text{PbB}_2^-$  (1),  $C_s$   $\text{PbB}_3\text{O}^-$  (2), and  $C_{2v}$   $\text{PbB}_4\text{O}_2^{-/0}$  (3 and 3'), NICS<sub>zz</sub>( $\zeta$ ) values of these clusters were calculated and compared with those of  $\text{B}_3^-$  clusters shown in Table 5. NICS values are usually calculated using the ring critical points,<sup>109,110</sup> but the  $\text{PbB}_2$  triangle does not have one. The centres of the ring currents (Fig. S6 and Table S2, ESI<sup>†</sup>) are used instead of the ring critical points. For these Pb/B species, all examined points located within or above the molecular planes possess large negative NICS<sub>zz</sub> values, and the NICS<sub>zz</sub> values decrease significantly as the  $\zeta$  values increase from 0 to 1 Å (Table 5). These phenomena appear to be similar to the computed NICS<sub>zz</sub> values for the prototypical  $\sigma + \pi$  doubly aromatic  $\text{B}_3^-$ . We conclude that  $C_{2v}$   $\text{PbB}_2^-$  (1),  $C_s$   $\text{PbB}_3\text{O}^-$  (2), and  $C_{2v}$   $\text{PbB}_4\text{O}_2^{-/0}$  (3 and 3') are  $\sigma + \pi$  doubly aromatic in nature, in agreement with the AdNDP results discussed above.

## 5.3 Multiple B–B bonding in $[\text{PbB}_2(\text{BO})_n]^-$ ( $n = 0-2$ )

According to the chemical bonding analyses shown in Fig. 8,  $[\text{PbB}_2(\text{BO})_n]^-$  ( $n = 0-2$ ) exhibit obvious multiple B–B bonding

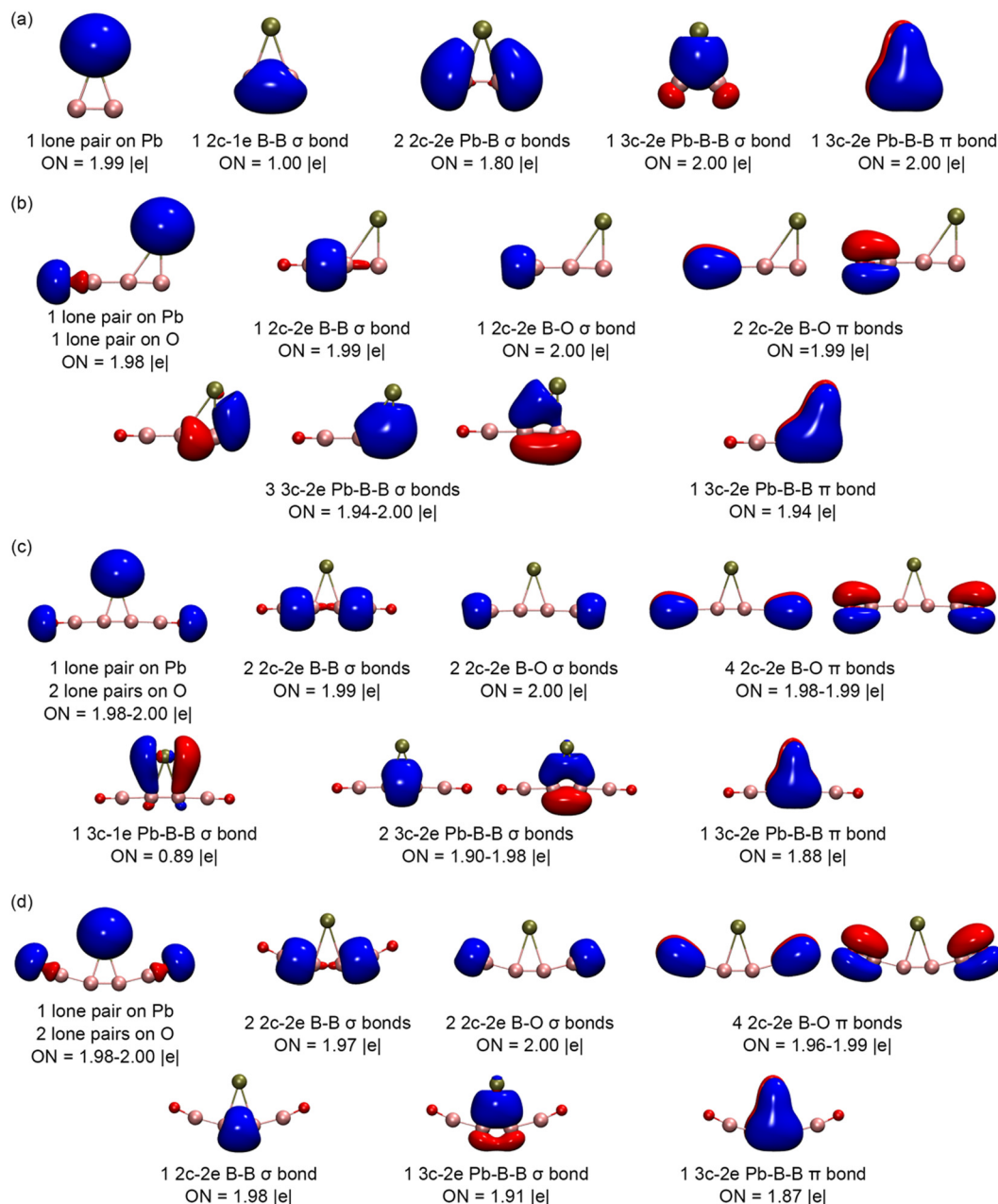


Fig. 8 AdNDP bonding analyses for the GM of (a)  $C_{2v}$   $PbB_2^-$  (**1**), (b)  $C_s$   $PbB_3O^-$  (**2**), (c)  $C_{2v}$   $PbB_4O_2^-$  (**3**), and (d)  $C_{2v}$   $PbB_4O_2$  (**3'**) at the PBE0/B<sub>3</sub>O/def2-TZVP/Pb/def2-TZVPP level. Isovalues for  $\sigma$  orbitals and  $\pi$  orbitals are 0.06 and 0.05, respectively. ON indicates the occupation numbers.

characteristics. With two 2c-2e Pb-B  $\sigma$  bonds, one 2c-1e B-B  $\sigma$  bond, and two delocalized 3c-2e  $\sigma/\pi$  bonds (Fig. 8a),  $C_{2v}$   $PbB_2^-$  (**1**) possesses two Pb-B single bonds and one B-B double bond with the NRT bond orders of 1.04 and 1.68 (Table S3, ESI<sup>†</sup>), respectively. The Pb-B bond length and B-B bond length in **1** are 2.283 Å and 1.553 Å (Fig. 4), respectively, in good accord with the Pb-B single-bond length (2.29 Å) and B=B double-bond length (1.56 Å) predicted from Pyykkö's additive atomic covalent radii,<sup>111</sup> respectively. Compared with the  $C_{2v}$   $PbB_2^-$  (**1**) which possesses three localized  $\sigma$  bonds (Fig. 8a),  $C_s$   $[PbB_2(BO)]^-$  (**2**) and  $C_{2v}$   $[PbB_2(BO)_2]^-$  (**3**) both have four delocalized  $\sigma/\pi$  bonds covered on their  $PbB_2$  cores (Fig. 8b and c), causing the Pb-B

bonding to be weakened, while the B-B bonds to be strengthened. The less symmetric **2** contains one weakened Pb-B bond with a NRT bond order of 0.63, one strengthened terminal Pb-B bond with a bond order of 1.55, and one strengthened B-B bond with a bond order of 1.78 (Table S3, ESI<sup>†</sup>). The terminal Pb-B bond length of 2.147 Å in **2** (Fig. 4) is consistent with the Pb=B double-bond length of 2.13 Å, based on Pyykkö's atomic covalent radii.<sup>111</sup> The central B-B bond length of 1.515 Å lies between the B=B double-bond length (1.56 Å) and the B≡B triple-bond length (1.46 Å) predicted by Pyykkö's atomic covalent radii.<sup>111</sup>

The two delocalized 3c-2e  $\sigma$  bonds and one delocalized 3c-2e  $\pi$  bond in the open-shell  $C_{2v}$   $PbB_4O_2^-$  (**3**) are mainly



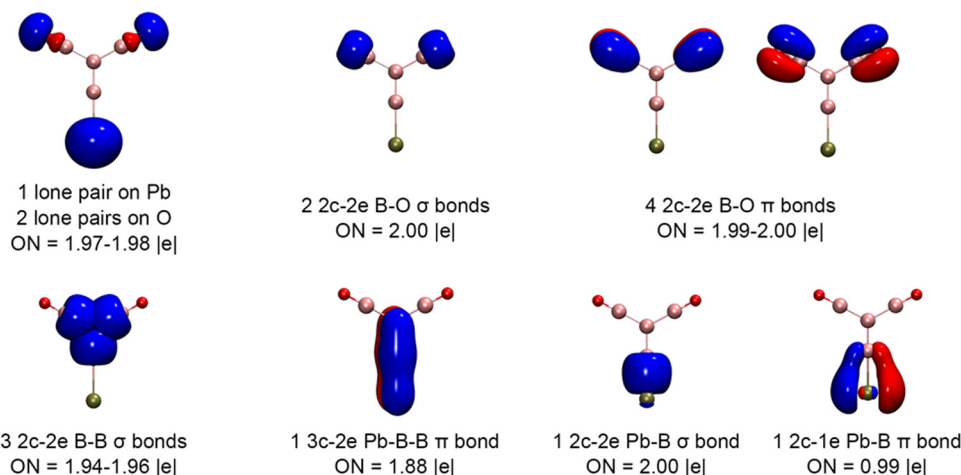


Fig. 9 The AdNDP bonding analysis for the Y-shaped  $C_{2v}$   $PbB_4O_2^-$  (**4**) at the PBE0/B<sub>3</sub>O/def2-TZVP/Pb/def2-TZVPP level. Isovalues for  $\sigma$  orbitals and  $\pi$  orbitals are 0.06 and 0.05, respectively. ON indicates the occupation numbers.

**Table 5** NICS<sub>zz</sub>( $\zeta$ ) values (ppm) of  $C_{2v}$   $PbB_2^-$  (**1**),  $C_s$   $PbB_3O^-$  (**2**),  $C_{2v}$   $PbB_4O_2^{-/0}$  (**3** and **3'**), and  $D_{3h}$   $B_3^-$  computed at the centres of the ring current using the ADF code with the PBE0/TZP all-electron basis, including the noncollinear spin-orbit coupling effect

	$PbB_2^-$	$PbB_3O^-$	$PbB_4O_2^-$	$PbB_4O_2$	$B_3^-$
$\zeta = 0.0$	−183.9	−136.4	−193.5	−209.1	−76.5
$\zeta = 0.2$	−173.4	−128.7	−185.3	−188.7	−74.2
$\zeta = 0.4$	−149.8	−111.5	−165.3	−144.3	−67.7
$\zeta = 0.6$	−126.0	−94.9	−142.0	−103.2	−58.6
$\zeta = 0.8$	−106.8	−82.1	−119.8	−75.4	−49.0
$\zeta = 1.0$	−90.4	−71.2	−99.4	−56.9	−40.0

concentrated on the B–B moiety of the  $PbB_2$  core (Fig. 8c). The central B–B bond with a NRT bond order of 1.76 is shortened to 1.498 Å (Fig. 4) which is close to the B≡B triple bond (1.46 Å) based on Pyykkö's atomic covalent radii. It is worth noting that the delocalized 3c-1e  $\sigma$  bond in **3** exhibits clearly partial anti-bonding nature, mainly derived from a Pb 6p orbital (Fig. 8c). With the unpaired electron detached, the length of the central B–B bond with the NRT bond order of 1.86 in neutral  $C_{2v}$   $PbB_4O_2^-$  (**3'**) is further shortened to 1.478 Å which can be approximately treated as a B≡B triple bond. In fact, the B≡B triple bond length in **3'** is slightly shorter than the corresponding value of 1.481 Å previously reported in the perfect linear  $D_{\infty h}$   $B_2(BO)_2^{2-}$  and slightly longer than that (1.468 Å) observed in  $D_{\infty h}$   $B_2(CO)_2$ .<sup>53,112</sup> Natural bonding orbital (NBO) analyses indicated that there exist substantial charge transfers from the Pb atoms to the  $B_4O_2$  units in  $C_{2v}$   $PbB_4O_2^{-/0}$  (**3** and **3'**) (0.45 |e| for **3**, 1.09 |e| for **3'**). Thus, these two charge-transfer complexes can be approximately viewed as  $Pb^+/Pb^{2+}$  units weakly interacting with the linear  $B_2(BO)_2^{2-}$  motifs, i.e.,  $Pb^+[B_2(BO)_2^{2-}]/Pb^{2+}[B_2(BO)_2^{2-}]$ , with Pb–B bond lengths (2.383 Å for **3**, 2.399 Å for **3'**; Fig. 4) obviously longer than the Pb–B single bond (2.29 Å).<sup>111</sup>

#### 5.4 Multiple Pb–B and B–B bonding in Y-shaped $PbB_4O_2^{-/2-}$

The structure of the low-lying Y-shaped isomer  $C_{2v}$   $PbB_4O_2^-$  (**4**) is interesting. Our AdNDP analysis for **4** (Fig. 9) showed the Pb

6s lone pair, two O lone pair lone pairs, two B≡O triple bonds, and two B–B≡O single bonds. The remaining valence electrons form one 2c-2e B–B  $\sigma$  bond, one 3c-2e B–B–Pb  $\pi$  bond, one 2c-2e Pb–B  $\sigma$  bond, and one 2c-1e Pb–B  $\pi$  bond, resulting in the B=B bond and the Pb–B bond along the two-fold main molecular axis which have the formal bond orders of 2.0 and 1.5, respectively. The B=B double bond length of 1.565 Å in **4** (Fig. 4) is comparable to the corresponding value of 1.56 Å obtained from Pyykkö's double-bond covalent atomic radii.<sup>111</sup> The Pb–B length of 2.195 Å lies between the Pb–B single bond length (2.29 Å) and the Pb=B double bond length (2.13 Å) computed from Pyykkö's covalent atomic radii, consistent with its formal bond order of 1.5. Adding an electron to **4** yields the closed-shell  $C_{2v}$   $PbB_4O_2^{2-}$  (**4'**, Fig. 4) with an even shortened Pb–B bond length of 2.188 Å, closer to a Pb=B double bond (2.13 Å).<sup>111</sup> Thus, the Y-shaped  $C_{2v}$   $PbB_4O_2^{2-}$  (**4'**) can be formulated as  $[Pb=B=B(B\equiv O)_2]^{2-}$ . NRT analyses predicted a B–B bond order of 1.59 for **4** and 1.69 for **4'**, which are slightly lower than 2.0 due to the existence of the delocalized B–B–Pb 3c-2e  $\pi$  bond. The calculated NRT bond orders for Pb–B in **4** and **4'** are 1.72 and 2.08, respectively, consistent with the 1.5 bond order for the Pb–B multiple bond in **4** and the Pb=B double bond in **4'**, respectively. The central B atom in **4'** undergoes  $sp^2$  hybridization and forms two single B–B bonds with the two boronyl ligands and a double bond with the B atom bonded to Pb. The B atom that is bonded to Pb undergoes  $sp$  hybridization, forming a Pb=B double bond and a B=B double bond, similar to the central C atom in the allene molecule ( $H_2C=C=CH_2$ ). In other words, the closed-shell  $C_{2v}$   $PbB_4O_2^{2-}$  (**4'**) is an electron-precise molecule with distinct hybridizations for the two central B atom and it is isovalent with  $Pb=C=CH_2$  and should be a highly stable species. However, the open-shell  $C_{2v}$   $PbB_4O_2^-$  (**4**) misses one electron, which may explain why it is less stable than the  $C_{2v}$  GM of  $PbB_4O_2^-$  (**3**). Nevertheless, it is conceivable that a large energy barrier may exist from isomer **4** to GM **3**, allowing **4** to be present in the experiment despite its relatively high energy.

## 6. Conclusion

In conclusion, we report an investigation on the structures and chemical bonding of three lead-boron clusters,  $\text{PbB}_2^-$ ,  $\text{PbB}_3\text{O}^-$ , and  $\text{PbB}_4\text{O}_2^-$ , using photoelectron spectroscopy and *ab initio* calculations. The global minima of these three species are found to be planar and can be formulated as  $[\text{PbB}_2(\text{BO})_n]^-$  ( $n = 0-2$ ), consisting of a triangular  $\text{PbB}_2$  core coordinated by zero, one, and two boronyl ligands, respectively. In addition, a Y-shaped low-lying isomer with a  $\text{Pb}=\text{B}=\text{B}$  unit coordinated by two BO ligands to the terminal B atom was also observed to be present in the cluster beam of  $\text{PbB}_4\text{O}_2^-$ . Chemical bonding analyses indicate that the global minima of  $\text{PbB}_2^-$  and  $\text{PbB}_3\text{O}^-$  have  $2\sigma/2\pi$  and  $6\sigma/2\pi$  delocalized electrons, respectively, rendering them doubly aromatic. The global minimum of the  $C_{2v}$   $\text{PbB}_4\text{O}_2^-$  contains  $5\sigma/2\pi$  delocalized electrons and is also shown to display double aromaticity. The Pb and  $\text{B}_2$  bonding is weak in the global minimum of  $\text{PbB}_4\text{O}_2^-$  and its corresponding neutral species of  $\text{PbB}_4\text{O}_2$ , which can be alternatively viewed as  $\text{Pb}^{+/2+}$  units coordinated to the linear  $\text{B}_4\text{O}_2^{2-}$  ligand with the  $\text{B}=\text{B}$  triple bond. The open-shell Y-shaped  $C_{2v}$   $\text{PbB}_4\text{O}_2^-$  isomer contains a Pb–B multiple bond with a bond order of 1.5, while the closed-shell Y-shaped  $\text{PbB}_4\text{O}_2^{2-}$  possesses a  $\text{Pb}=\text{B}$  double bond with the bond order of 2.0, which is an electron-precise molecule with distinct hybridization for the two B atoms,  $[\text{Pb}=\text{B}=\text{B}(\text{BO})_2]^{2-}$ . Investigation of the lead-boron cluster enriches the understanding of Pb–B bonding and provides new insights for the rational design of novel Pb–B molecules and potential lead boride materials.

## Author contributions

W. J. C. and T. T. C. performed the experiments. Q. C., X. Y. W., R. N. Y., and H. G. L. performed the computational calculations. S. D. L. and L. S. W. guided the work. Q. C., W. J. C., D. F. Y., S. D. L., and L. S. W. wrote and revised the manuscript. All authors analyzed the experimental and theoretical results.

## Conflicts of interest

The authors declare no conflicts of interest.

## Acknowledgements

We thank Dr H. S. Hu for help with the NICSzz calculations. This work was supported by the US National Science Foundation (CHE-2053541 to L.S.W.) and the National Natural Science Foundation of China (22003034 to Q. C., 21973057 and 21720102006 to S.D.L.). Q.C. gratefully acknowledges the start-up fund from Shanxi University for the support.

## References

- W. N. Lipscomb, *Science*, 1977, **196**, 1047.
- E. D. Jemmis and D. L. V. K. Prasad, *J. Solid State Chem.*, 2006, **179**, 2768.

- B. Albert and H. Hillebrecht, *Angew. Chem., Int. Ed.*, 2009, **48**, 8640.
- A. N. Alexandrova, A. I. Boldyrev, H. J. Zhai and L. S. Wang, *Coord. Chem. Rev.*, 2006, **250**, 2811.
- E. Oger, N. R. Crawford, R. Kelting, P. Weis, M. M. Kappes and R. Ahlrichs, *Angew. Chem., Int. Ed.*, 2007, **46**, 8503.
- A. P. Sergeeva, I. A. Popov, Z. A. Piazza, W. L. Li, C. Romanescu, L. S. Wang and A. I. Boldyrev, *Acc. Chem. Res.*, 2014, **47**, 1349.
- L. S. Wang, *Int. Rev. Phys. Chem.*, 2016, **35**, 69.
- W. L. Li, X. Chen, T. Jian, T. T. Chen, J. Li and L. S. Wang, *Nat. Rev. Chem.*, 2017, **1**, 0071.
- M. R. Fagiani, X. Song, P. Petkov, S. Debnath, S. Gewinner, W. Schöllkopf, T. Heine, A. Fielicke and K. R. Asmis, *Angew. Chem., Int. Ed.*, 2017, **56**, 501.
- T. Jian, X. Chen, S. D. Li, A. I. Boldyrev, J. Li and L. S. Wang, *Chem. Soc. Rev.*, 2019, **48**, 3550.
- H. J. Zhai, Y. F. Zhao, W. L. Li, Q. Chen, H. Bai, H. S. Hu, Z. A. Piazza, W. J. Tian, H. G. Lu, Y. B. Wu, Y. W. Mu, G. F. Wei, Z. P. Liu, J. Li, S. D. Li and L. S. Wang, *Nat. Chem.*, 2014, **6**, 727.
- Q. Chen, W. L. Li, Y. F. Zhao, S. Y. Zhang, H. S. Hu, H. Bai, H. R. Li, W. J. Tian, H. G. Lu, H. J. Zhai, S. D. Li, J. Li and L. S. Wang, *ACS Nano*, 2015, **9**, 754.
- Y. J. Wang, Y. F. Zhao, W. L. Li, T. Jian, Q. Chen, X. R. You, T. Ou, X. Y. Zhao, H. J. Zhai, S. D. Li, J. Li and L. S. Wang, *J. Chem. Phys.*, 2016, **144**, 064307.
- H. R. Li, T. Jian, W. L. Li, C. Q. Miao, Y. J. Wang, Q. Chen, X. M. Luo, K. Wang, H. J. Zhai, S. D. Li and L. S. Wang, *Phys. Chem. Chem. Phys.*, 2016, **18**, 29147.
- W. J. Chen, Y. Y. Ma, T. T. Chen, M. Z. Ao, D. F. Yuan, Q. Chen, X. X. Tian, Y. W. Mu, S. D. Li and L. S. Wang, *Nanoscale*, 2021, **13**, 3868.
- T. T. Chen, L. F. Cheung and L. S. Wang, *Annu. Rev. Phys. Chem.*, 2022, **73**, 233.
- J. Barroso, S. Pan and G. Merino, *Chem. Soc. Rev.*, 2022, **51**, 1098.
- C. Romanescu, T. R. Galeev, W. L. Li, A. I. Boldyrev and L. S. Wang, *Acc. Chem. Res.*, 2013, **46**, 350.
- W. L. Li, A. S. Ivanov, J. Federic, C. Romanescu, I. Cernusak, A. I. Boldyrev and L. S. Wang, *J. Chem. Phys.*, 2013, **139**, 104312.
- L. F. Cheung, G. S. Kocheril, J. Czekner and L. S. Wang, *J. Phys. Chem. A*, 2020, **124**, 2820.
- L. F. Cheung, G. S. Kocheril, J. Czekner and L. S. Wang, *J. Am. Chem. Soc.*, 2020, **142**, 3356.
- L. F. Cheung, J. Czekner, G. S. Kocheril and L. S. Wang, *J. Am. Chem. Soc.*, 2019, **141**, 17854.
- Q. Chen, H. J. Zhai, S. D. Li and L. S. Wang, *J. Chem. Phys.*, 2013, **138**, 084306.
- W. J. Chen, M. Kulichenko, H. W. Choi, J. Cavanagh, D. F. Yuan, A. I. Boldyrev and L. S. Wang, *J. Phys. Chem. A*, 2021, **125**, 6751.
- T. T. Chen, W. L. Li, H. Bai, W. J. Chen, X. R. Dong, J. Li and L. S. Wang, *J. Phys. Chem. A*, 2019, **123**, 5317.
- C. Romanescu, T. R. Galeev, A. P. Sergeeva, W. L. Li, L. S. Wang and A. I. Boldyrev, *J. Organomet. Chem.*, 2012, **721**, 148.

- 27 T. R. Galeev, C. Romanescu, W. L. Li, L. S. Wang and A. I. Boldyrev, *Angew. Chem., Int. Ed.*, 2012, **51**, 2101.
- 28 W. L. Li, C. Romanescu, T. R. Galeev, Z. A. Piazza, A. I. Boldyrev and L. S. Wang, *J. Am. Chem. Soc.*, 2012, **134**, 165.
- 29 C. Romanescu, T. R. Galeev, W. L. Li, A. I. Boldyrev and L. S. Wang, *Angew. Chem., Int. Ed.*, 2011, **50**, 9334.
- 30 T. R. Galeev, C. Romanescu, W. L. Li, L. S. Wang and A. I. Boldyrev, *J. Chem. Phys.*, 2011, **135**, 104301.
- 31 I. A. Popov, W. L. Li, Z. A. Piazza, A. I. Boldyrev and L. S. Wang, *J. Phys. Chem. A*, 2014, **118**, 8098.
- 32 B. Le Chen, W. G. Sun, X. Y. Kuang, C. Lu, X. X. Xia, H. X. Shi and G. Maroulis, *Inorg. Chem.*, 2018, **57**, 343.
- 33 M. Ren, S. Jin, D. Wei, Y. Y. Jin, Y. Tian, C. Lu and G. L. Gutsev, *Phys. Chem. Chem. Phys.*, 2019, **21**, 21746.
- 34 W. L. Li, T. T. Chen, W. J. Chen, J. Li and L. S. Wang, *Nat. Commun.*, 2021, **12**, 6467.
- 35 T. T. Chen, W. L. Li, T. Jian, X. Chen, J. Li and L. S. Wang, *Angew. Chem., Int. Ed.*, 2017, **56**, 6916.
- 36 W. L. Li, T. Jian, X. Chen, T. T. Chen, G. V. Lopez, J. Li and L. S. Wang, *Angew. Chem., Int. Ed.*, 2016, **55**, 7358.
- 37 T. Jian, W. L. Li, X. Chen, T. T. Chen, G. V. Lopez, J. Li and L. S. Wang, *Chem. Sci.*, 2016, **7**, 7020.
- 38 W. L. Li, T. T. Chen, Z. Y. Jiang, W. J. Chen, H. S. Hu, L. S. Wang and J. Li, *Chin. J. Chem. Phys.*, 2019, **32**, 241.
- 39 W. L. Li, T. Jian, X. Chen, H. R. Li, T. T. Chen, X. M. Luo, S. D. Li, J. Li and L. S. Wang, *Chem. Commun.*, 2017, **53**, 1587.
- 40 T. Jian, W. L. Li, I. A. Popov, G. V. Lopez, X. Chen, A. I. Boldyrev, J. Li and L. S. Wang, *J. Chem. Phys.*, 2016, **144**, 154310.
- 41 I. A. Popov, T. Jian, G. V. Lopez, A. I. Boldyrev and L. S. Wang, *Nat. Commun.*, 2015, **6**, 8654.
- 42 C. Xu, L. Cheng and J. Yang, *J. Chem. Phys.*, 2014, **141**, 124301.
- 43 T. T. Chen, W. L. Li, W. J. Chen, X. H. Yu, X. R. Dong, J. Li and L. S. Wang, *Nat. Commun.*, 2020, **11**, 2766.
- 44 W. J. Chen, Y. Y. Zhang, W. L. Li, H. W. Choi, J. Li and L. S. Wang, *Chem. Commun.*, 2022, **58**, 3134.
- 45 M. Kulichenko, W. J. Chen, H. W. Choi, D. F. Yuan, A. I. Boldyrev and L. S. Wang, *J. Vac. Sci. Technol., A*, 2022, **40**, 042201.
- 46 A. I. Boldyrev and L. S. Wang, *Phys. Chem. Chem. Phys.*, 2016, **18**, 11589.
- 47 H. J. Zhai, A. N. Alexandrova, K. A. Birch, A. I. Boldyrev and L. S. Wang, *Angew. Chem., Int. Ed.*, 2003, **42**, 6004.
- 48 A. P. Sergeeva, D. Y. Zubarev, H. J. Zhai, A. I. Boldyrev and L. S. Wang, *J. Am. Chem. Soc.*, 2008, **130**, 7244.
- 49 D. Y. Zubarev and A. I. Boldyrev, *J. Comput. Chem.*, 2007, **28**, 251.
- 50 H. J. Zhai, L. M. Wang, S. D. Li and L. S. Wang, *J. Phys. Chem. A*, 2007, **111**, 1030.
- 51 H. Braunschweig, K. Radacki and A. Schneider, *Science*, 2010, **328**, 345.
- 52 M. Zhou, N. Tsumori, Z. Li, K. Fan, L. Andrews and Q. Xu, *J. Am. Chem. Soc.*, 2002, **124**, 12936.
- 53 S. D. Li, H. J. Zhai and L. S. Wang, *J. Am. Chem. Soc.*, 2008, **130**, 2573.
- 54 L. C. Ducati, N. Takagi and G. Frenking, *J. Phys. Chem. A*, 2009, **113**, 11693.
- 55 H. Braunschweig, R. D. Dewhurst, K. Hammond, J. Mies, K. Radacki and A. Vargas, *Science*, 2012, **336**, 1420.
- 56 H. J. Zhai, S. D. Li and L. S. Wang, *J. Am. Chem. Soc.*, 2007, **129**, 9254.
- 57 W. Z. Yao, J. C. Guo, H. G. Lu and S. D. Li, *J. Phys. Chem. A*, 2009, **113**, 2561.
- 58 D. Y. Zubarev, A. I. Boldyrev, J. Li, H. J. Zhai and L. S. Wang, *J. Phys. Chem. A*, 2007, **111**, 1648.
- 59 H. J. Zhai, J. C. Guo, S. D. Li and L. S. Wang, *Chem. Phys. Chem.*, 2011, **12**, 2549.
- 60 Q. Chen, H. Bai, H. J. Zhai, S. D. Li and L. S. Wang, *J. Chem. Phys.*, 2013, **139**, 044308.
- 61 Q. Chen, H. J. Zhai, S.-D. Li and L. S. Wang, *J. Chem. Phys.*, 2012, **137**, 044307.
- 62 H. Bai, H. J. Zhai, S. D. Li and L. S. Wang, *Phys. Chem. Chem. Phys.*, 2013, **15**, 9646.
- 63 H. J. Zhai, C. Q. Miao, S. D. Li and L. S. Wang, *J. Phys. Chem. A*, 2010, **114**, 12155.
- 64 H. J. Zhai, Q. Chen, H. Bai, H. G. Lu, W. L. Li, S. D. Li and L. S. Wang, *J. Chem. Phys.*, 2013, **139**, 174301.
- 65 T. T. Chen, L. F. Cheung, W. J. Chen, J. Cavanagh and L. S. Wang, *Angew. Chem., Int. Ed.*, 2020, **59**, 15260.
- 66 T. Jian, L. F. Cheung, T. T. Chen and L. S. Wang, *Angew. Chem., Int. Ed.*, 2017, **56**, 9551.
- 67 L. F. Cheung, T. T. Chen, G. S. Kocheril, W. J. Chen, J. Czekner and L. S. Wang, *J. Phys. Chem. Lett.*, 2020, **11**, 659.
- 68 W. J. Tian, W. J. Chen, M. Yan, R. Li, Z. H. Wei, T. T. Chen, Q. Chen, H. J. Zhai, S. D. Li and L. S. Wang, *Chem. Sci.*, 2021, **12**, 8157.
- 69 H. Liu, S. Wang, G. Zhou, J. Wu and W. Duan, *J. Chem. Phys.*, 2007, **126**, 134705.
- 70 A. Kumar, *Radiat. Phys. Chem.*, 2017, **136**, 50.
- 71 D. K. Gaikwad, S. S. Obaid, M. I. Sayyed, R. R. Bhosale, V. V. Awasarmol, A. Kumar, M. D. Shirsat and P. P. Pawar, *Mater. Chem. Phys.*, 2018, **213**, 508.
- 72 M. I. Sayyed, Y. S. Rammah, A. S. Abouhaswa, H. O. Tekin and B. O. Elbashir, *Phys. B*, 2018, **548**, 20.
- 73 S. Woosley, N. Abuali Galehdari, A. Kelkar and S. Aravamudhan, *J. Mater. Res.*, 2018, **33**, 3657.
- 74 X. Li, J. Wu, C. Tang, Z. He, P. Yuan, Y. Sun, W.-M. Lau, K. Zhang, J. Mei and Y. Huang, *Composites, Part B*, 2019, **159**, 355.
- 75 Y. Wu, Q. P. Zhang, D. Zhou, Y. L. Zhou and J. Zheng, *J. Alloys Compd.*, 2017, **727**, 1027.
- 76 W. J. Chen, T. T. Chen, Q. Chen, H. G. Lu, X. Y. Zhao, Y. Y. Ma, Q. Q. Yan, R. N. Yuan, S. D. Li and L. S. Wang, *Commun. Chem.*, 2022, **5**, 25.
- 77 L. S. Wang, H. S. Cheng and J. Fan, *J. Chem. Phys.*, 1995, **102**, 9480.
- 78 A. P. Sergeeva, B. B. Averkiev, H. J. Zhai, A. I. Boldyrev and L. S. Wang, *J. Chem. Phys.*, 2011, **134**, 224304.
- 79 C. Adamo and V. Barone, *J. Chem. Phys.*, 1999, **110**, 6158.
- 80 W. R. Wadt and P. J. Hay, *J. Chem. Phys.*, 1985, **82**, 284.

- 81 P. J. Hay and W. R. Wadt, *J. Chem. Phys.*, 1985, **82**, 299.
- 82 P. J. Hay and W. R. Wadt, *J. Chem. Phys.*, 1985, **82**, 270.
- 83 K. A. Peterson, *J. Chem. Phys.*, 2003, **119**, 11099.
- 84 R. A. Kendall, T. H. Dunning and R. J. Harrison, *J. Chem. Phys.*, 1992, **96**, 6796.
- 85 J. Čížek, *Adv. Chem. Phys.*, 1969, **14**, 35.
- 86 G. D. Purvis and R. J. Bartlett, *J. Chem. Phys.*, 1982, **76**, 1910.
- 87 K. Raghavachari, G. W. Trucks, J. A. Pople and M. Head-Gordon, *Chem. Phys. Lett.*, 1989, **157**, 479.
- 88 G. E. Scuseria, C. L. Janssen and H. F. Schaefer III, *J. Chem. Phys.*, 1988, **89**, 7382.
- 89 G. E. Scuseria and H. F. Schaefer, *J. Chem. Phys.*, 1989, **90**, 3700.
- 90 H. J. Werner and P. J. Knowles, *J. Chem. Phys.*, 1985, **82**, 5053.
- 91 P. Celani and H. J. Werner, *J. Chem. Phys.*, 2000, **112**, 5546.
- 92 H. J. Werner and P. J. Knowles, *J. Chem. Phys.*, 1988, **89**, 5803.
- 93 A. Berning, M. Schweizer, H. J. Werner, P. J. Knowles and P. Palmieri, *Mol. Phys.*, 2000, **98**, 1823.
- 94 D. Y. Zubarev and A. I. Boldyrev, *Phys. Chem. Chem. Phys.*, 2008, **10**, 5207.
- 95 W. Humphrey, A. Dalke and K. Schulten, *J. Mol. Graphics*, 1996, **14**, 33.
- 96 P. v R. Schleyer, C. Maerker, A. Dransfeld, H. Jiao and N. J. R. V. E. Hommes, *J. Am. Chem. Soc.*, 1996, **118**, 6317.
- 97 E. Van Lenthe and E. J. Baerends, *J. Comput. Chem.*, 2003, **24**, 1142.
- 98 C. Foroutan-Nejad, J. Vicha and A. Ghosh, *Phys. Chem. Chem. Phys.*, 2020, **22**, 10863.
- 99 L. Alvarado-Soto, R. Ramírez-Tagle and R. Arratia-Pérez, *Chem. Phys. Lett.*, 2008, **467**, 94.
- 100 E. Schott, X. Zárate and R. Arratia-Pérez, *Polyhedron*, 2011, **30**, 846.
- 101 E. D. Glendening and F. Weinhold, *J. Comput. Chem.*, 1998, **19**, 593.
- 102 E. D. Glendening, C. R. Landis and F. Weinhold, *J. Comput. Chem.*, 2019, **40**, 2234.
- 103 M. J. Frisch, G. W. Trucks and H. B. Schlegel *et al.*, *GAUSSIAN 09, Revision A.2*, Gaussian, Inc., Wallingford, CT, 2009.
- 104 H. J. Werner, P. J. Knowles, G. Knizia, F. R. Manby, M. Schütz, P. Celani, T. Korona, R. Lindh, A. Mitrushenkov, G. Rauhut *et al.*, *MOLPRO*, version 2012.1.
- 105 ADF and SCM, Theoretical Chemistry, Vrije Universiteit, Amsterdam, The Netherlands, 2014, <https://www.scm.com>.
- 106 H. Fliegl, S. Taubert, O. Lehtonen and D. Sundholm, *Phys. Chem. Chem. Phys.*, 2011, **13**, 20500.
- 107 P. Pykkö, *Chem. Rev.*, 1988, **88**, 563.
- 108 W. J. Chen, M. Kulichenko, H. W. Choi, J. Cavanagh, D. F. Yuan, A. I. Boldyrev and L. S. Wang, *J. Phys. Chem. A*, 2021, **125**, 6751.
- 109 C. Foroutan-Nejad, S. Shahbazian and P. Rashidi-Ranjbar, *Phys. Chem. Chem. Phys.*, 2010, **12**, 12630.
- 110 C. Foroutan-Nejad, Z. Badri, S. Shahbazian and P. Rashidi-Ranjbar, *J. Phys. Chem. A*, 2011, **115**, 12708.
- 111 P. Pykkö, *J. Phys. Chem. A*, 2015, **119**, 2326.
- 112 M. Zhou, N. Tsumori, Z. Li, K. Fan, L. Andrews and Q. Xu, *J. Am. Chem. Soc.*, 2002, **124**, 12936.